Lawrence Berkeley National Laboratory
LBL Publications

Title
Tensiometry in fractured rocks

Permalink
https://escholarship.org/uc/item/9jv6242r

Author
Faybishenko, Boris

Publication Date
1999-07-01

eScholarship.org Powered by the California Digital Library
University of California

LBNL-43864

ERNEST ORLANDO LAWRENCE
BERKELEY NATIONAL LABORATORY

On the Physics of Tensiometry in Fractured Rocks

Boris Faybishenko and Stefan Finsterle

Earth Sciences Division

July 1999

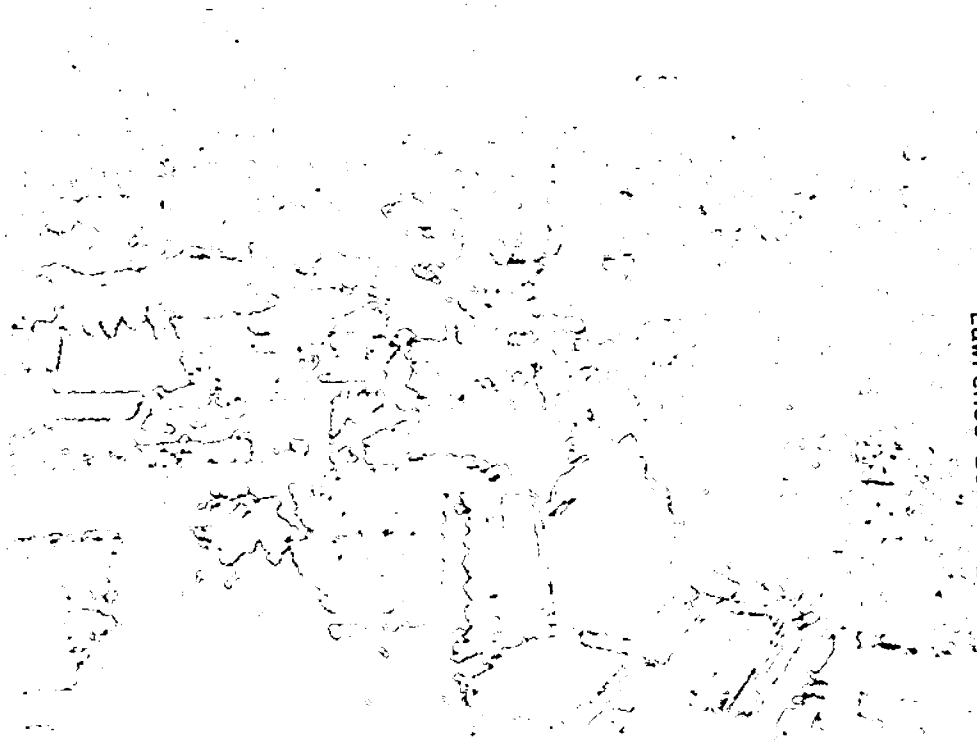

REFERENCE COPY
Does Not
Circulate
Bldg. 50 Library - Ref.
Lawrence Berkeley National Laboratory
Copy 1

LBNL-43864

DISCLAIMER

This document was prepared as an account of work sponsored by the United States Government. While this document is believed to contain correct information, neither the United States Government nor any agency thereof, nor the Regents of the University of California, nor any of their employees, makes any warranty, express or implied, or assumes any legal responsibility for the accuracy, completeness, or usefulness of any information, apparatus, product, or process disclosed, or represents that its use would not infringe privately owned rights. Reference herein to any specific commercial product, process, or service by its trade name, trademark, manufacturer, or otherwise, does not necessarily constitute or imply its endorsement, recommendation, or favoring by the United States Government or any agency thereof, or the Regents of the University of California. The views and opinions of authors expressed herein do not necessarily state or reflect those of the United States Government or any agency thereof or the Regents of the University of California.

LBNL-43864

On the Physics of Tensiometry in Fractured Rocks

Boris Faybishenko and Stefan Finsterle

Earth Sciences Division
Ernest Orlando Lawrence Berkeley National Laboratory
University of California
Berkeley, California 94720

July 1999

This work was funded by the Office of Environmental Management, Office of Science and Technology, Characterization, Monitoring, and Sensor Technology Crosscutting Program, and the Environmental Management Science Program of the U.S. Department of Energy under Contract No. DE-AC03-76SF00098.

On the Physics of Tensiometry in Fractured Rocks

Boris Faybishenko and Stefan Finsterle
E.O. Lawrence Berkeley National Laboratory
Berkeley, CA 94720

Abstract

One of the challenging problems of vadose zone hydrologic investigations is the determination of water pressure in unsaturated fractured rocks. Tensiometers are commonly used under both laboratory and field conditions for measuring the water pressure in variably saturated porous and fractured media. In order to improve our understanding of tensiometer measurement physics, we present a concept of tensiometry, analyze the results of laboratory and field infiltration tests in fractured basalt, and compare the laboratory experimental data with a numerically simulated response of tensiometers in a fractured-porous medium. We show that the water pressure in the most conductive hydraulic component of the media (at the time of measurement) primarily affects the tensiometer gauge-pressure: during imbibition, the pressure measured by the tensiometer represents the fracture water pressure, whereas during drainage, it represents the matrix water pressure. During drainage, the measured water pressure is representative of average rock saturation, but not during imbibition. Thus, tensiometer measurements can exhibit significant extrinsic hysteresis even without taking into account the intrinsic hysteresis of the unsaturated hydraulic characteristics of the matrix and fracture. Because of the complex three-dimensional, channelized preferential water flow, local water pressure measurements using tensiometers are of limited use for the evaluation of hydraulic gradient and water flux in fractured rocks on the field scale. The tensiometer measurements can provide only a limited understanding of the water travel time and the fracture-matrix interaction in fractured rocks, and should be supplemented by other types of measurements under field conditions.

Introduction

One of the challenging problems of vadose-zone hydrologic investigations is the determination of water potential in unsaturated-saturated heterogeneous soils and fractured rocks. The water potential is a characteristic of the energy status of water in the subsurface. Tensiometers have been widely used under both laboratory and field conditions in variably saturated porous media to assess the soil water potential, which is then used to determine the hydraulic gradient, direction of water flow, and the water flux in soils, as well as to indirectly estimate the soil water content using water retention curves (Sposito, 1981; ASTM, 1998; Kutilek and Nielsen, 1994). Unfortunately, only little experience is available from fractured rock investigations (Schneebeli et al., 1995; Gimmi et al., 1996; Persoff and Pruess, 1995; Hubbell and Sisson, 1998; Tokunaga, 1997). Field, laboratory, and modeling studies of water flow in heterogeneous soils and rocks showed that water flows not as a single sheet, but rather exhibits a complex three-dimensional, channelized preferential flow pattern (Glass et al., 1989a, 1989b; Pruess, 1999; Su et al., 1999). Because of low permeability of a rock matrix, water and chemicals may bypass the matrix and move rapidly through fractures to the underlying aquifer. This behavior was shown both experimentally (Nativ et al., 1995; Flint and Flint, 1995) and numerically (Pruess, 1999).

The objective of this paper is to improve our understanding on the physics of tensiometry in fractured rocks and to investigate whether tensiometer measurements of water pressure in heterogeneous fractured-porous media can be used to directly assess the water flow field, including the hydraulic gradient, water flux, and the moisture content of fractured rocks.

We first present theoretical concepts of tensiometry in a fractured-porous media and the results of a laboratory experiment on a fractured basalt core, followed by numerical simulations of water flow in fractured-porous media. Then, we analyze the field data of a ponded infiltration test in fractured basalt conducted at the Box Canyon site, Idaho, near the Idaho National Engineering and Environmental Laboratory (INEEL). Finally, we present a concept of the extrinsic hysteresis of tensiometry in fractured rocks.

Concept of Tensiometer Measurements in Fractured-Porous Media

Conceptual Model of the System Fractured Rock-Tensiometer. Fractured rock can be represented as a two-domain medium of fractures and matrix, often called fractured-porous medium. Figure 1 schematically shows that when a porous tip of a tensiometer intersects both fractures and the porous matrix, we have to consider a three-domain system *fractured rock-tensiometer*. The fracture domain (fractures are often infilled with sediments) can also be characterized as a porous medium with corresponding water retention and unsaturated hydraulic conductivity functions (Pruess and Tsang, 1990; Pruess, 1999).

A typical feature of flow in unsaturated rocks is a multi-scale channeling effect that is observed on a small scale (centimeters) within single fractures, an intermediate scale (from centimeters to meters) within a fracture network, and a large scale (up to hundreds of meters) involving several basalt flows (Faybishenko et al., 1999b). Because the length of a tensiometer porous tip ranges from a few to 20 centimeters, a single tensiometer provides water potential measurements that are affected by local water seeps, which are in contact with the porous tip surface area. Water channeling in fractures may create faster flow in fractures in comparison with the matrix. Several attempts were made to explain the phenomenon of fast water seepage in fractured rocks using concepts of film flow (Tokunaga and Wan, 1997) and water channeling (Johns and Roberts, 1991; Pruess, 1999; Su et al., 1999). Because of water channeling in fractures, the diffusive coupling between the fracture and matrix occurs only within a small area of the fracture plane (Dykhuizen, 1992; Su et al., 1999). Ho (1997) showed that pendant water droplets in fractured tuffaceous rock exist near asperities and cavities as a result of gravity-dominated flow through fractures.

Hallaire (1961) was probably the first who, contrary to a conventional soil-science point of view, raised the concern that the volume-averaged water potential and moisture

content measured in structured soils are not suitable for an analysis of water flow and transport. He explained his results using a scheme similar to that shown in Figure 2, which depicts a network of water-conducting channels within the matrix. This scheme shows that under transient conditions of evaporation, water potentials, which are point-type measurements (Slattery, 1971), are different in fractures and the matrix. The local difference in water potentials leads to a three-dimensional fracture-matrix water exchange.

Schematic of Tensiometer Measurements. A tensiometer tip, which intersects both the fracture and matrix, will represent a weighted-average water potential of both the fracture and matrix water potentials, which are different under transient water flow conditions. Figure 3 shows a schematic of tensiometer measurements in variably saturated fractured-porous media under drying and wetting conditions. A conventional tensiometer consists of a fine porous (ceramic or metal) tip filled with water and connected to a manometer through a water-filled tube. For shallow tensiometer measurements, the water-filled tube is extended to the surface. A small volume of air (a few cubic centimeters) is usually present in the top portion of this tube. This design is called an air-pocket tensiometer (Villa Nova et al., 1989). From a mechanistic point of view, assuming the coupled flow processes in a three-domain system consisting of the fractured-porous rock and a tensiometer, the expression for the tensiometer water pressure, P, averaged over the surface area of a tensiometer porous tip, is given by

$$P = \alpha P_{\mathrm{m}} + \beta P_{\mathrm{f}} + \Delta P_{\mathrm{t}} \qquad (1)$$

where P_{m} and P_{f} are, respectively, the matrix and fracture, capillary pressure (when $P < 0$ for unsaturated conditions) or water pressure (when $P \geq 0$ for saturated conditions); α and β are dimensionless coefficients, with $\alpha + \beta = 1$; and ΔP_t is the term that takes into account air-bubble volume-pressure changes, which occur in the air-pocket tensiometer as affected by diurnal temperature fluctuations, and the local water redistribution around the tensiometer tip (Buchter et al., 1999). The capillary pressures P_m and P_f are nonlinear functions of the moisture content, and in general they are significantly different for the

unsaturated fracture and matrix. Our results presented here will show that the contribution of fracture and matrix pressures to the total pressure measured by a tensiometer may vary under drying and wetting conditions, thus leading to hysteresis in the tensiometer data even without consideration of the intrinsic hysteretic characteristics of water retention and hydraulic conductivity curves.

Under drying conditions with no water in the fracture, it can be assumed that the gauge pressure corresponds to the capillary pressure of the matrix surrounding the porous tip (Figure 3a). Under wetting conditions, the fracture that contacts the porous tip may become saturated resulting in a positive water pressure, $P_f > 0$, which is no longer dependent on the moisture content. Despite the matrix capillary pressure, $P_m < 0$, the tensiometer pressure immediately increases because of the positive water pressure in the fracture (Figure 3b). As a result, the measured tensiometer pressure does not relate directly to the average volumetric moisture content of the surrounding formation. Moreover, the saturated porous tip offers resistance to water seepage, and the interaction between the fractured-porous formation and the tensiometer tip is supposed to locally change the liquid and air flow pattern. Under drying conditions, when the fracture is drained, the matrix capillary forces mostly control the measured total water potential, while under wetting conditions, the water pressure in a water-conducting fracture may significantly increase the total water potential.

Changes in the water pressure of the surrounding media create the hydraulic gradient and water exchange between the formation and the tensiometer. This water exchange depends on the hydraulic conductivity of both the tensiometer tip and the fractured-porous medium, as well as the volume of the air-bubble in the tensiometer. When the hydraulic conductivity of the medium is high (assuming high permeability of the tensiometer tip), the water exchange is fast, the time-delay of the tensiometer measurements is small. For a low hydraulic conductivity formation, temperature variations may affect both pressure and air-volume fluctuations that are not balanced with the water exchange between the tensiometer and the formation. The magnitude of diurnal

pressure fluctuations caused by ambient temperature fluctuations is likely to be a qualitative indicator of the formation's hydraulic conductivity.

Laboratory Experiment and Modeling

Laboratory Experiment. A laboratory experiment was performed on a basalt core with a single vertical fracture taken from the TAN site of the Idaho National Engineering and Environmental Laboratory (Finsterle and Faybishenko, 1998). A schematic of the experimental apparatus is shown in Figure 4. The cylindrical core 10 cm high and 5 cm in diameter was equipped with top and bottom porous ceramic plates (high-flow, air-entry pressure of 1 bar, manufactured by Soil Moisture, Inc., Santa Barbara, CA). Four horizontal tensiometers (diameter 0.6 cm, length 2.5 cm, high-flow, air entry pressure of 1 bar) were installed at two levels near the top and bottom of the core. At each level, we installed one tensiometer in the matrix and the other intersecting the fracture. All tensiometers were connected to differential pressure transducers DP-15 and an automatic data acquisition system. Water was injected from the bottom into the initially air-dry core for two hours, with a pressure head equivalent to the height of the core. When water reached the top of the core, a suction of -90 kPa was applied at the bottom porous plate, draining the system. Figure 5 shows tensiometer pressures measured during imbibition and drainage. During imbibition (Figure 5a), the tensiometers intersecting the fracture showed a faster response than the matrix tensiometers. The quick response of the fracture tensiometers is a result of fast water flow through the fracture, which was followed by slower water redistribution into the matrix. During drainage (Figure 5b), the responses of the fracture and matrix tensiometers are qualitatively similar and slower compared with their respective responses during imbibition. The laboratory results were analyzed using numerical modeling and then related to the field observations described below.

Model Assumptions. The performance of a tensiometer under conditions of two-phase flow of water and air in the fractured rock was numerically simulated using the

TOUGH2 code (Pruess, 1991). In order to investigate the interaction between the fractured-porous medium and the tensiometer, we simulated water flow between the fracture, matrix, tensiometer tip, and tubing. Figure 6 shows the discretization of the tensiometer having a fully saturated porous cup (air-entry pressure of 1 bar) with the inner water-filled chamber, tubing, and a small gas bubble. Pressure changes in the rock result in water in- and outflow through the tensiometer tip, leading to a slight compression or expansion of the air bubble in the tensiometer. The air-bubble pressure was considered the tensiometer gauge pressure.

Flow in the core was considered two-dimensional, with locally three-dimensional flow around the ceramic tips. Richards equation with van Genuchten's water retention and unsaturated hydraulic conductivity models were solved using integral finite differences. The main parameters of the fractured-porous medium and the tensiometer used in the simulation of the laboratory experiment are summarized in Table 1 and Figure 7.

Simulation Results. Figure 8 shows the water saturation and the flow direction distributions 15 minutes and two hours after beginning of imbibition and drainage. Figure 8a shows that during injection, water quickly flows through the highly permeable fracture, from where it imbibes horizontally into the matrix. Imbibition into the matrix also occurs axially from the bottom boundary, saturating almost the entire core within two hours. Figure 8b shows that the reverse process, i.e., drainage to the bottom boundary, is much less efficient because the fracture is emptied almost immediately. During drainage, the unsaturated fracture becomes a capillary barrier for water drained from the matrix. Consequently, drainage has to occur through the matrix alone, requiring a longer time period for desaturation despite the much stronger pressure gradient. Note in Figure 8 that the flow field in the core is slightly affected by the presence of the tensiometers, which, in turn, affects the measured pressure. The simulation results shown in Figure 8 also indicate that the asymmetry of the fracture plane with respect to the core axis and geometrical boundaries creates a two-dimensional flow field and nonuniform

saturation distribution, for which there are no analytical solutions describing the flow experiment.

Figure 9 shows the comparison of the gauge pressure in the two lower tensiometers, which are compared with the actual (numerically determined) capillary pressure in the fracture and matrix at the same level. Immediately after starting imbibition, the fracture capillary pressure increases to zero. At this time, the contribution of the matrix pressure is negligible ($\alpha \sim 0$). The tensiometer intersecting the fracture responds almost instantaneously as observed in the laboratory experiment. In other words, a tensiometer is capable of accurately depicting the arrival of water in a fracture. However, water flow from the fracture to the tensiometer and into the matrix, as well as the compressibility of the tensiometer air bubble, lead to a slower later-time increase in the fracture tensiometer pressure compared with the actual pressure in the fracture. Even if the tensiometer sensitivity were increased by reducing system compliance and flow resistance of the tensiometer tip, the transient tensiometer pressure may, nevertheless, differ from the fracture capillary pressure because the porous tip contacts the matrix as well. The difference between the matrix tensiometer reading and the actual matrix capillary pressure can be attributed to suboptimal tensiometer sensitivity.

Notice that the tensiometer pressures reached slight positive values, reflecting the positive water pressure encountered as a result of the imposed boundary hydraulic head. Figure 9 shows that during drainage, the tensiometers measure the matrix capillary pressure because the relative contribution of the capillary pressure in a low moisture content fracture is negligible ($\beta \sim 0$).

Field observations

Characteristics of the Fracture Network. Field investigations were conducted at the Box Canyon site in Idaho near the INEEL (Faybishenko et al., 1999a,b). The geological discontinuities, which significantly affect water flow in fractured basalt, are subvertical column-bounding fractures, which are also called joints (Engelder, 1987;

Priest, 1993), intra-basalt fractures, fracture zones, and rubble zones. Column-bounding fractures in basalt usually form a polygonal network within a basalt flow. At the Box Canyon site, the average spacing between basalt columnar joints is approximately 0.5 m at the surface, 2.0 m near the center of the basalt flow, and 1.3 m at the bottom. The maximum spacing near the center of the flow is 4.5 m. The tributary structure of the fracture pattern suggests a possibility of flow funneling and cascading from many shallow fractures to fewer fractures with depth (Figure 10). As a result, multiple flow paths may lead to a given point.

Characteristics of Ponded Infiltration Test. Several ponded infiltration tests were conducted in 1996-98 at the Box Canyon site using a surface pond of 7 by 8 m over the central portion of a basalt flow. The infiltration test analyzed in this paper is a two-week test conducted in 1996 under a constant water level of approximately 23 cm, described in detail in Faybishenko et al. (1999a). The initial infiltration rate was 11 cm/day, decreasing gradually after two weeks to less than 2 cm/day, presumably because of mechanical or microbiological clogging of fractures and vesicular basalt in the near-surface zone, as well as the effect of entrapped air.

The subsurface moisture redistribution was monitored in boreholes with tensiometers, neutron logging, and ground penetrating radar (GPR). Neutron logging and GPR survey showed several local zones of increased moisture content during ponding. However, because these methods are based on using manually operated probes, they could not be used to determined the water travel time in fractured rocks.

Water pressure measurements to a depth of 3 m were conducted using air-pocket tensiometers (with an air bubble of 2-3 cm^3) at 23 locations in eight boreholes within the pond and three boreholes outside the pond. The tensiometers were connected to the automatic data acquisition system with measurements every 6 minutes. Table 2 summarizes the installation depths of tensiometers and the lithology. This table also shows the first arrival time of water during the infiltration test determined from tensiometer measurements.

Tensiometry During the Ponded Infiltration Test. In order to illustrate the tensiometer responses obtained in a fractured basalt system, we summarize in Figure 11 tensiometer measurements in eleven boreholes at depths of 0.3-0.6 m, 1.5-1.8 m, and 2.7-3 m, conducted before, during, and after the two-week ponded infiltration test. This figure shows that all tensiometers exhibited diurnal fluctuations of the measured water pressure before the infiltration test. Such fluctuations indicate that the ambient temperature fluctuations affected the pressure of the small tensiometer air bubble, because the water exchange between the tensiometers and low hydraulic conductivity unsaturated rocks was limited. Figure 12, taken from Hubbell and Sisson (1998), who compared the performance of a conventional air-pocket and an advanced tensiometer (without an air bubble), reveals that the time-averaged water pressure of the conventional air-pocket tensiometer is a reliable estimate of the water pressure in the formation.

Figure 11 shows that during surface flooding, the water pressure increased and remained constant with time at all tensiometers at the depth of 0.3-0.6 m. The disappearance of diurnal tensiometer pressure fluctuations indicates that the hydraulic conductivity increased significantly, leading to a rapid water exchange between the tensiometer and the surrounding formation. The moment of the first increase in the tensiometer pressure represents the time of water arrival at the tensiometer location. (We assume that the temporal rock mechanical effects and air pressure propagation are negligible.) In the interval 1.5-1.8 m, the tensiometers exhibited both rapid (Boreholes T-2, T-4, and T-9) and delayed (Boreholes T-6, T-7, and T-8) water arrivals within 0.5-3 days. The delayed water arrival suggests slower and indirect routes of water travel. In the interval 2.7-3 m, there were two rapid water arrivals (T-8 and T-9) and two gradual arrivals (T-4 and T-5), and the remaining tensiometers exhibited diurnal fluctuations suggesting that infiltrating water did not arrive at these locations.

Figure 13 shows an expanded view of the time variation of water pressure at the beginning of flooding and immediately after the end of flooding. In contrast to the almost instantaneous response of tensiometers at the beginning of flooding, the pressure

responses after the end of ponding occurred much more slowly. This behavior is similar to that observed in the laboratory core (see Figure 5) and determined from the modeling study (see Figure 9). Thus, the field data confirmed that under flooding conditions the tensiometer response in fractured-porous media is determined by flow through fractures, followed by matrix imbibition.

It can be seen from Figures 11 and 13 that before the infiltration test, the water pressure was mostly negative at depths of 0.3-0.6 and 1.5-1.8 m, indicating unsaturated flow conditions. During ponding, the tensiometers that measured a positive water pressure (9 of 10 tensiometers at 0.3-0.6 m, and 6 of 8 at 1.5-1.8 m depths) indicated the presence of local perched water zones or pendant water in fractured basalt. Examination of pressure curves also shows the gradual decrease of the tensiometer pressure and the reappearance of pressure fluctuations during the infiltration test (Well T-8, depths 1.8 and 2.7 m, and Well T-5, depth 3 m). These results suggest that some fractures that were saturated early in the tests might have become desaturated thereafter even under conditions of ponded infiltration.

Figure 14 illustrates the water arrival times within the upper 3-m zone and shows a significant scatter of data, indicating that only a range of water arrival times (shown by the lines "First arrival" and "Late arrival") can be determined using local tensiometer measurements.

Figure 15 shows that at greater depths, fewer tensiometers were affected by infiltrating water. The decrease with depth in the number of tensiometers affected by infiltrating water is consistent with the concept of funneling in a single basalt flow, which leads to fewer water-flow paths with depth. Figure 15 also illustrates the decrease in the fracture frequency with depth. Note that the number of tensiometers affected by infiltrating water can also decrease with depth because of a dendritic pattern of water flow in a spatially correlated permeability field representing a heterogeneous medium (Pruess, 1999).

Thus, the analysis of tensiometer data showed evidence of preferential flow rather than the propagation of a uniform wetting front. Because tensiometers are located in different parts of basalt with significantly different unsaturated and saturated hydraulic conductivities, and are affected by three-dimensional channeling effects, local tensiometer pressures cannot be used to calculate the hydraulic gradient needed to determine the direction of water flow on the field scale in fractured-porous media. Other types of measurements conducted at the Box Canyon site (neutron logging, time domain reflectometry, and ground-penetrating radar) confirmed a complex three-dimensional flow pattern (Faybishenko et al., 1999a).

Extrinsic Hysteresis in Fracture Rock Tensiometry

Because of the water exchange between fractures and the matrix, tensiometer data show a hysteretic loop that we will call extrinsic. We use the term *extrinsic hysteresis* in order to distinguish the hysteresis occurring in a fracture-matrix-tensiometer system from the intrinsic hysteresis of formation materials themselves. The hysteretic effect makes the application of an ordinary thermodynamics questionable (Sposito, 1981, p. 203). Figure 16 shows the fracture and matrix water-retention curves, which we used to determine the volume-averaged water retention curve under equilibrium conditions. Assuming the same water pressure in both the matrix and the fracture, the volume-averaged water saturation for pressure P is given by

$$S_{va} = \frac{\Theta_{va}}{\phi_m + \phi_f} = \phi_m S_m(P) + \phi_f S_f(P) \qquad (2)$$

where S_{va} and Θ_{va} are volume-averaged saturation and water content, respectively, ϕ_f is the fracture porosity, and ϕ_m is the matrix porosity. In calculating the curves in Figure 16, we used the same parameters as in the numerical model of the laboratory experiment described above (see Table 1). One can see in Figure 16 that for the same pressure P_c, there are three different saturation values - fracture saturation S_f, matrix saturation S_m, and the volume-averaged saturation S_{va}. It can be seen that the matrix and volume-

averaged water-retention curves are close to each other. This is because the fracture porosity used in this calculation (ϕ_f=0.02) is much less than that for the matrix (ϕ_m=0.23) (Faybishenko et al., 1999a).

Laboratory, field, and modeling studies confirmed that when water flowing along a zone of preferential flow reaches the tensiometer tip, the fracture water pressure increases the tensiometer pressure. This increase in tensiometer pressure is accompanied by a slight initial increase of the moisture content of the fractured rock because of low fracture porosity. To illustrate this concept, the dashed line in Figure 16 shows a transient water-retention curve of the fracture-matrix-tensiometer system. This curve was plotted using the results of the laboratory experiment described above (see Figure 5). In Figure 16, the pressure registered by the upper fracture tensiometer before the test is depicted on the volume-averaged water-retention curve, and the increase in pressure and volume-averaged rock saturation is shown as a circle. Thus, water imbibition causes a significant shift of the water retention curve from the volume-averaged toward the fracture water-retention curve. However, because of imbibition into the matrix and local redistribution of water around the tensiometer tip, the water-retention curve for the saturation event will not reach the fracture water-retention curve. These data indicate that conventional neutron logging in fractured rocks in boreholes, which provides volume-averaged measurements, may not detect changes in rock saturation as affected by water flow through a fracture network.

Contrary to the saturation process, the difference between the volume-averaged curve and matrix water-retention curve is small during the drainage event (Figure 16), which implies that the drainage water-retention curve will be located between these two curves. Water discharge has to occur primarily through the matrix, requiring a longer time for desaturation.

Conclusions

The water pressure in the most conductive hydraulic component of a fractured-porous medium primarily affects the tensiometer gauge-pressure: during imbibition, the pressure measured by the tensiometer corresponds to the fracture water pressure, whereas during drainage, it represents the matrix water pressure. Thus, tensiometer measurements can exhibit significant hysteresis even without taking into account the intrinsic hysteresis of the water retention and unsaturated hydraulic conductivity characteristics of the matrix and fractures.

Laboratory measurements and the numerical simulation of water flow in a fractured core showed that the asymmetry of flow geometry with respect to the core axis and geometrical boundaries leads to a complex distribution of the moisture content and the flow field in the core. This makes conventional one-dimensional analytical solutions impractical for estimating hydraulic properties of fractured cores. In order to analyze the results of laboratory experiments on single fractured cores, we recommend two-dimensional inverse modeling.

Because the tensiometers provide local measurements of water pressure in the subsurface, they can give only limited qualitative understanding of the geometry and physics of water flow in the subsurface. For example, if a tensiometer tip intersects the fracture, it can depict the water arrival through the fracture. The sharp increase in pressure immediately after the beginning of surface flooding suggests that fracture flow is relatively fast and that the water pulse is registered with a short response time of the tensiometer.

In summary, field, laboratory, and modeling studies showed that the volume-averaged, local tensiometer measurements of water pressure might lead to erroneous interpretations if used directly to assess the hydraulic gradient, direction of water flow, and moisture content of fractured rocks. Because of the extrinsic hysteresis, the contribution of the fracture and matrix water pressures remains unknown, and an

averaged water pressure cannot be determined based on the assumption of equilibrium. Therefore, the accurate analysis of the results of field measurements requires the application of inverse modeling techniques.

Acknowledgment: The authors would like to thank Peter Persoff and Michael Steiger for participation in the laboratory experiment. Reviews and suggestions for improvement by Peter Persoff and André Unger, as well as discussions with Tetsu Tokunaga are very much appreciated. This work was funded by the Office of Environmental Management, Office of Science and Technology, Characterization, Monitoring, and Sensor Technology Crosscutting Program, and the Environmental Management Science Program of the U.S Department of Energy under Contract No. DE-AC03-76SF00098.

References

ASTM 3404-91, Standard Guide for Measuring Matric Potential in the Vadose Zone Using Tensiometers, American Society for Testing and Materials, West Conshohochken, PA, 1998.

Buchter, B., C. Hinz, H. Wydler, H. Fluehler, Evaluation of temperature and bypass flow sensitivity of tensiometers in a field soil, *Geoderma, 87*(3-4), 281-291, 1999.

Dykhuizen, R. C., Diffusive matrix fracture coupling including the effects of flow channeling, *Water Resour. Res., 28*(9), 2447-2450, 1992.

Engelder, T., Joints and shear fractures in rock, in *Fracture Mechanics of Rock*, edited by B.K. Atkinson, pp. 27-69, Academic Press, Orlando, FL, 1987.

Faybishenko, B., C. Doughty, S. Steiger, J. Long, T. Wood, J. Jacobsen, J. Lore, and P. Zawislanski, Conceptual model of the geometry and physics of water flow in a fractured

basalt vadose zone: Box Canyon site, Idaho, Report LBNL-42925 (Paper submitted to *Water Resources Research*), 1999a.

Faybishenko, B., P. A. Witherspoon, C. Doughty, T. Wood, R. Podgorney, and J. Geller, Multi-scale investigations of liquid flow in a fractured basalt vadose zone, Report LBNL-42910 (Paper submitted to the AGU Monograph "*Flow and Transport in Fractured Rocks*), 1999b.

Finsterle, S., and B. Faybishenko, What does a tensiometer measure in fractured rocks? Report LBNL-41454, (In print, *Proceedings of the International Conference "Characterization and Measurement of the Hydraulic Properties of Unsaturated Porous Media*"), 1998.

Flint, L.E., and A.L. Flint, Shallow infiltration processes at Yucca Mountain – Neutron logging data, 1984-93, US Geological Survey Open-File Report 95-4035, 46 p., 1995.

Gimmi, T., M. Schneebeli, H. Flühler, H. Wydler, and T. Baer, Field-scale water transport in unsaturated crystalline rock, *Water Resour. Res.,* 33(4), 589-598, 1996.

Glass, R.J., J.-Y. Parlange, and T.S. Steenhuis, Wetting front instability: 1. Theoretical discussion and dimensional analysis, *Water Resour. Res.*, 25, 1187-1194, 1989a.

Glass, R.J., J.-Y. Parlange, and T.S. Steenhuis, Wetting front instability: 2. Experimental determination of relationship between system parameters and two-dimentional unstable flow field behavior in initially dry porous media, *Water Resour. Res.*, 25, 1195-1207, 1989b.

Hallaire, M., Irrigation et utilisation reserves naturelles. Ann. Agr., v.12, No.1, 1961.

Ho, C.K., Evaporation of pendant water droplets in fractures, *Water Resour. Res., 33*(12), 2665-2671, 1997.

Hubbell, J.M., and J.B. Sisson, Advanced tensiometer for shallow or deep soil water potential measurements, *Soil Sci., 163*(4), 271-277, 1998.

Johns, R.A. and P.V. Roberts, A solute transport model for channelized flow in a fracture, *Water Resour. Res., 27*(8), 1797-1808, 1991.

Kutilek, M. and D. R. Nielsen, *Soil Hydrology*, Catena Verlag, Germany, 1994.

Nativ, R., E. Adar, O. Dahan, and M. Geyh, Water recharge and solute transport through the vadose zone of fractured chalk under desert conditions, *Water Resour. Res., 31*(2), 253-261, 1995.

Persoff, P., and K. Pruess, Two-phase flow visualization and relative permeability measurement in natural rough-walled rock fractures, *Water Resour. Res., 31*(5), 1175-1186, 1995.

Priest, S.D., *Discontinuity Analysis for Rock Engineering*, Chapman and Hall, London, 1993.

Pruess, K., A mechanistic model for water seepage through thick unsaturated zones in fractured rocks of low matrix permeability, *Water Resour. Res.*, 35 (4), 1039-1051, 1999.

Pruess, K. and Y. W. Tsang, On two-phase relative permeability and capillary pressure of rough-walled rock fractures, *Water Resour. Res., 26*(9), 1915-1926, 1990.

Pruess, K. TOUGH2 - A General Purpose Numerical Simulator for Multiphase Fluid and Heat Flow, Report LBL-29400, Lawrence Berkeley Laboratory, Berkeley, CA, May 1991.

Schneebeli, M., H. Flühler, T. Gimmi, H. Wydler, H.-P. Läser, and T. Baer, Measurements of water potential and water content in unsaturated crystalline rock, *Water Resour. Res.*, *31*(8), 1837-1843, 1995.

Slattery, J.C., *Momentum, Energy, and Mass Transfer in Continua*, McGraw-Hill, New York, 1971.

Sposito, G., *The Thermodynamics of Soil Solutions*, Oxford, New York, Oxford University Press, 1981.

Su, G.W., J.T. Geller, K. Pruess, and F. Wen, Experimental studies of water seepage and intermittent flow in unsaturated, rough-walled fractures, *Water Resour. Res.*, *35*(4), 1019-1037, 1999.

Tokunaga, T.K., A tensiometer for measuring hydraulic potentials on surfaces of porous rock, *Water Resour. Res.*, *33*(6), 1509-1513, 1997.

Tokunaga, T.K., and J. Wan, Water film flow along fracture surfaces of porous rock, *Water Resour. Res.* *33*(6), 1287-1295, 1997.

Villa Nova, N.A., K. Reichardt, P.L. Libardi, and S.O. Moraes, Direct reading "air-pocket" tensiometer, *Soil Technology*, *2*, pp. 403-407.

Figure Captions

Figure 1. Schematic showing a three-domain system of fracture-matrix medium with a tensiometer, showing a tensiometer porous tip inserting both the fracture and matrix, and a tensiometer porous tip inserting the matrix.

Figure 2. A network of water-conducting channels intersecting the matrix, which have different water potentials, Ψ, on the micro-scale (after Hallaire, 1961).

Figure 3. Schematic of tensiometer measurements in variably saturated fractured-porous media under drying and wetting conditions using a U-type water manometer. Note that under drying conditions $P = f(\Theta_m)$, and under wetting conditions $P \neq f(\Theta)$.

Figure 4. Schematic of the laboratory experimental apparatus for measuring water flow in a fractured core during drying and wetting.

Figure 5. Time variations of tensiometer pressures determined in a laboratory experiment on a fractured basalt core showing (a) the fast response during imbibition, and (b) the slower response during drainage. Note the different vertical scale of water pressures in figures (a) and (b).

Figure 6. Scheme (not to scale) of the discretization of the tensiometer components (porous cup, tubing, and the air bubble) and the surrounding matrix and fracture used for modeling. The model is locally three-dimensional around the porous cup.

Figure 7. Curves of (a) water retention, and (b) unsaturated hydraulic conductivity for the fracture and matrix materials calculated using parameters given in Table 1 and used in numerical modeling of flow in a fractured basalt core.

Figure 8. Saturation distribution and liquid flow directions 15 minutes and 2 hours after the beginning of imbibition (a) and drainage (b).

Figure 9. Results of modeling showing the comparison of water pressures determined in the fracture and matrix with water pressures determined with the fracture and matrix tensiometers.

Figure 10. A portion of a two-dimensional fracture map of the Box Canyon outcrop (Faybishenko et al., 1999a) showing the location of the infiltration pond and several hypothetical directions (thick lines) of water flow along column-bounding fractures leading to funneling and cascading effects.

Figure 11. Time variations of water pressure at three depths before, during, and after a two-week ponded infiltration test at the Box Canyon site at depths 0.3-0.6 m, 1.5-1.8 m, and 2.7-3 m. The bottom figure shows the time variation of the ambient temperature.

Figure 12. Comparison of water pressure measured using a conventional air-pocket tensiometer and an advanced tensiometer without an air bubble (Hubbell and Sisson, 1998).

Figure 13. Expanded view of the time variation of water pressure at depths of 0.3-0.6 m and 1.5-1.8 m at the beginning and the end of the infiltration test.

Figure 14. The results of determination of water arrival times after the beginning of flooding using tensiometers.

Figure 15. Comparison of plots of the percent of tensiometers detected infiltrating water with the percent of normalized fracture frequency. (Note that the fracture frequency was normalized to the fracture frequency at the depth of 0.4 m, which was determined from borehole investigations.)

Figure 16. Water retention curves for fracture and matrix, as well as the volume-averaged water retention curve for fractured basalt calculated using Equation (2) and parameters given in Table 1. The solid circle indicates the change in Θ and P immediately after the fracture saturation.

Table 1. Parameters used in simulation of flow in the fractured basalt core

	Basalt Core		Tensiometer	
Parameter	**Matrix**	**Fracture**	**Ceramic Cup**	**Tubing**
Permeability (m^2)	1.0E-14	1.0E-10	1.0E-16	1.0E-9
Porosity	0.23	-	0.30	1.00
Aperture (mm)	-	0.10	-	-
Air entry pressure (Pa)	2.0E3	2.0E1	1.0E5	0.0
Van Genuchten *n*	1.47	1.47	-	-
Initial saturation	0.39	0.03	1.00	1.00

Table 2. Summary of lithology and water arrival times for tensiometers used to monitor the infiltration test at the Box Canyon site

Depths 0.3-0.6 m

Well	Depth (m)	Lithology	Time of infiltrating water arrival since the begging of flooding (days)
I-1	0.3	High angle fracture in vesicular basalt	0.120
I-2	0.3	Vesicular basalt	0.016
I-3	0.3	Low angle fractures in vesicular basalt	0.016
T-5	0.3	Vesicular basalt	0.026
T-8	0.3	Low and high angle fractures	0.022
T-9	0.3	Vesicular basalt	0.016
T-2	0.6	Vesicular basalt	0.448
T-3	0.6	Vesicular basalt	0.256
T-4	0.6	Vesicular basalt with widely spaced vesicles	0.303
T-7	0.6	Vesicular basalt	0.016

Depths 1.5-1.8 m

Well	Depth (m)	Lithology	Time of infiltrating water arrival since the begging of flooding (days)
T-4	1.5	Horizontal fracture in massive basalt	0.481
T-5	1.5	Vesicular basalt	No arrival
T-8	1.5	High angle fracture in massive basalt	1.026
T-9	1.5	Vesicular basalt	0.020
T-2	1.8	Massive basalt with a large vesicle	0.598
T-3	1.8	Vesicular bend in massive basalt with a large vesicle	No arrival
T-6	1.8	Massive basalt	0.752
T-7	1.8	Low angle and horizontal fractures in massive basalt	1.833

Table 2 - Continued

Depths 2.7-3 m

Well	Depth (m)	Lithology	**Time of infiltrating water arrival since the begging of flooding (days)**
T-4	2.7	Vesicular basalt with large vesicles	0.752
T-8	2.7	Low angle fracture in massive and vesicular basalt	0.481
T-2	3	Low angle fracture in massive basalt	No arrival
T-3	3	Horizontal fracture in vesicular basalt	No arrival
T-5	3	Vesicular basalt	1.25
T-6	3	Low angle fracture in massive basalt	No arrival
T-7	3	Massive basalt	No arrival
T-9	3	Horizontal fracture in massive basalt	0.066

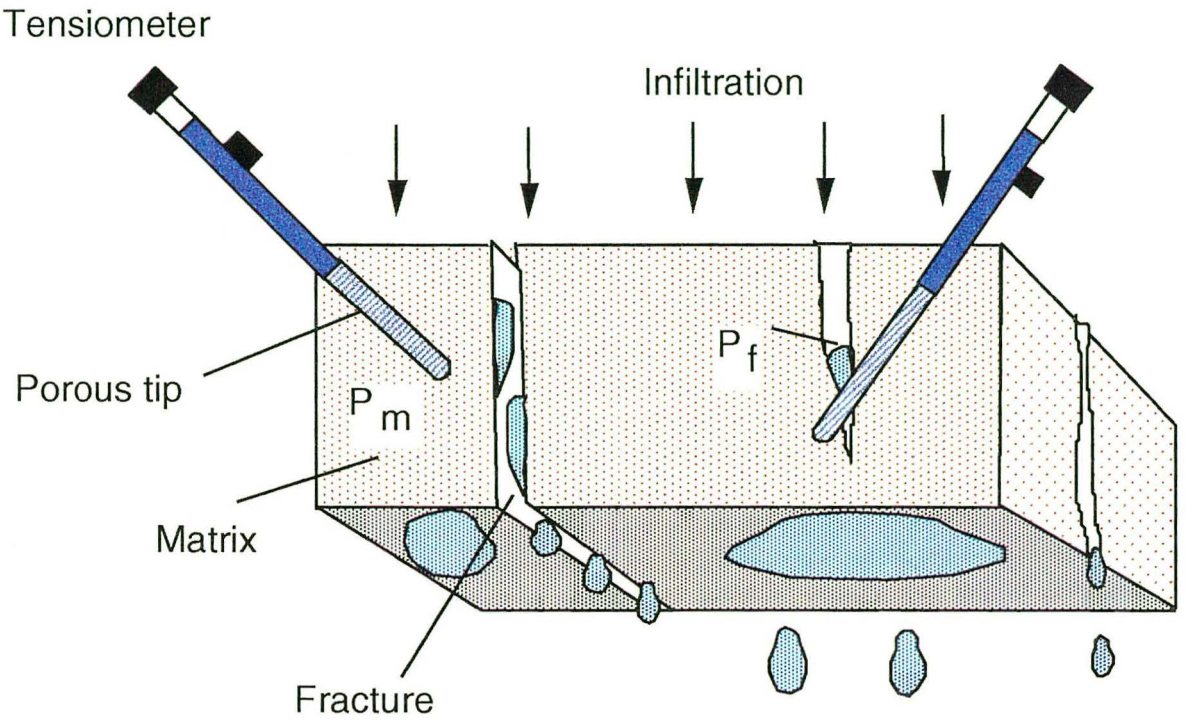
Tensiometer
Infiltration
Porous tip
P m
P f
Matrix
Fracture

Figure 1

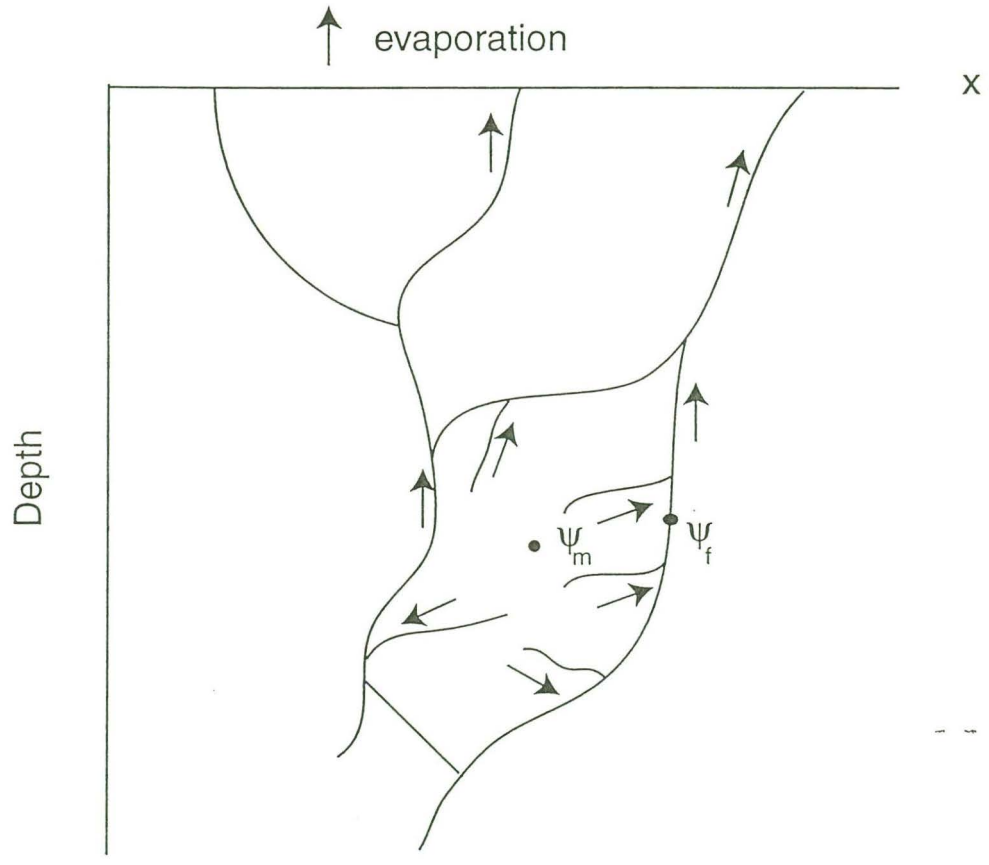

Figure 2

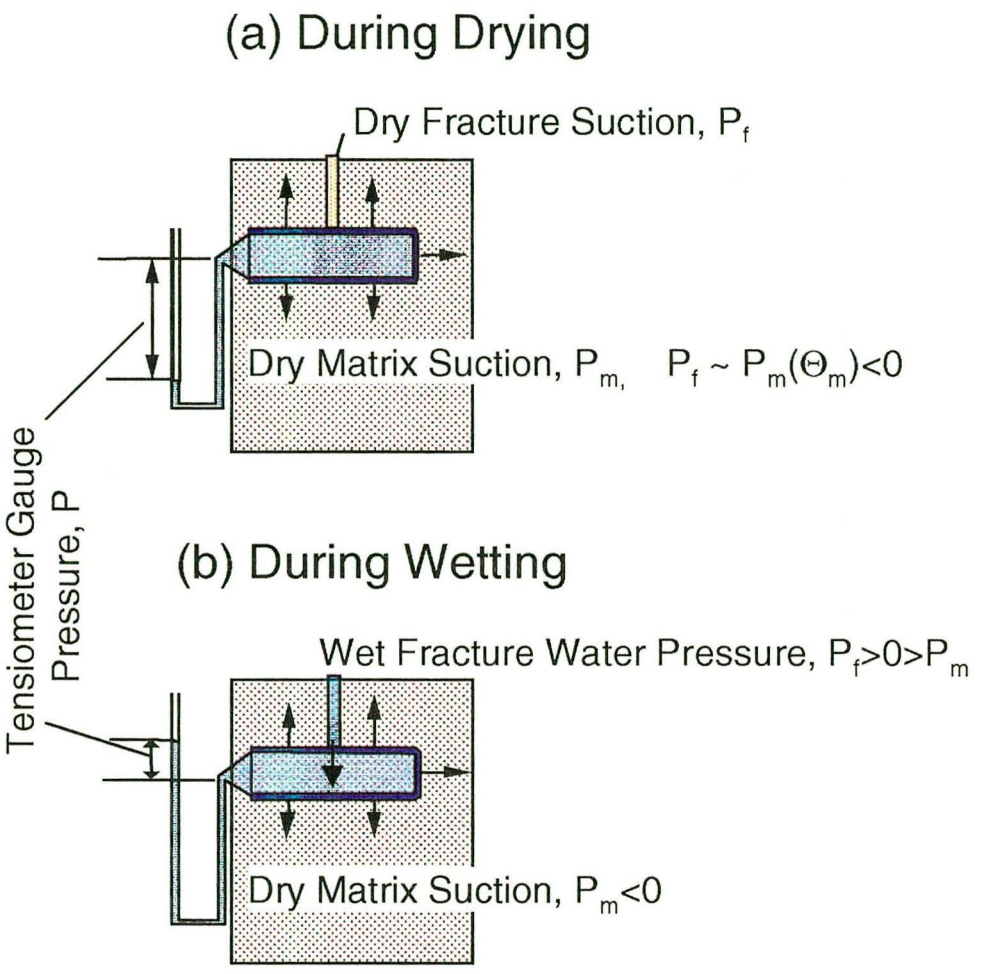
(a) During Drying
Dry Fracture Suction, P_f
Dry Matrix Suction, $P_{m,}$ $P_f \sim P_m(\Theta_m)<0$
Tensiometer Gauge Pressure, P
(b) During Wetting
Wet Fracture Water Pressure, $P_f>0>P_m$
Dry Matrix Suction, $P_m<0$

Figure 3.

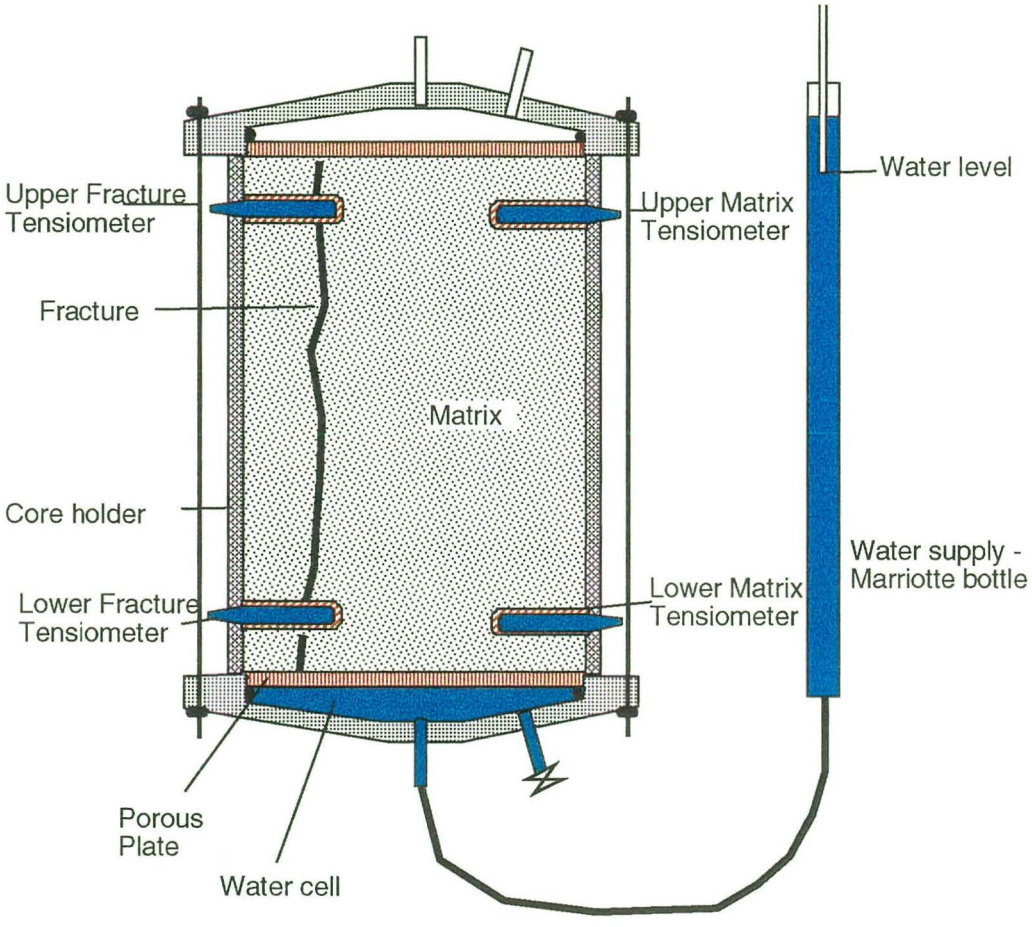
Upper Fracture Tensiometer
Upper Matrix Tensiometer
Water level
Fracture
Matrix
Core holder
Water supply - Marriotte bottle
Lower Fracture Tensiometer
Lower Matrix Tensiometer
Porous Plate
Water cell

Figure 4

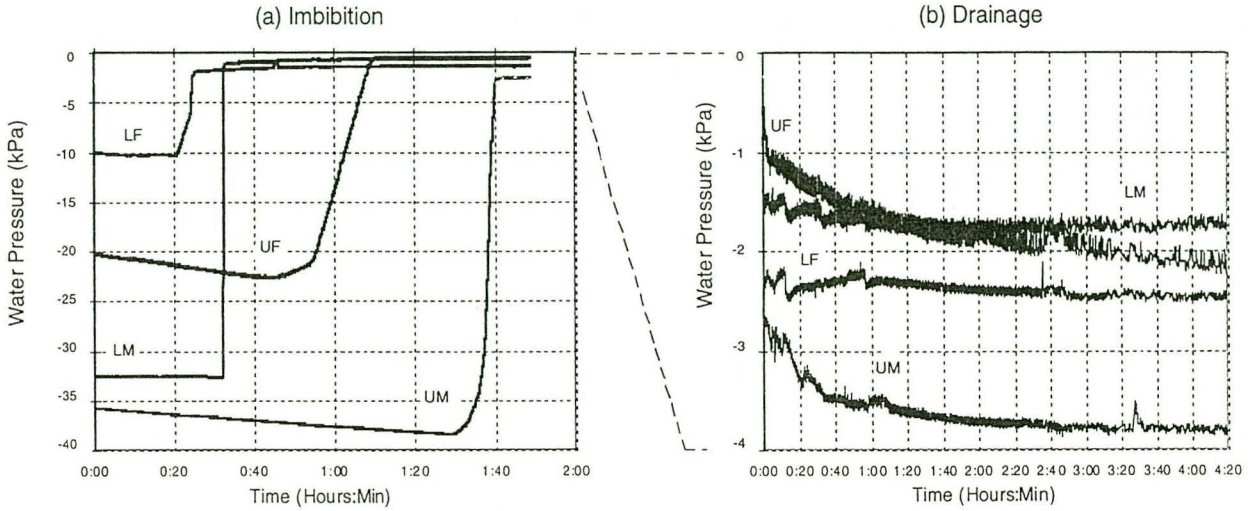
(a) Imbibition
(b) Drainage
Water Pressure (kPa)
Time (Hours:Min)
LF
UF
LM
UM
0
-5
-10
-15
-20
-25
-30
-35
-40
0:00
0:20
0:40
1:00
1:20
1:40
2:00
-1
-2
-3
-4
0:00 0:20 0:40 1:00 1:20 1:40 2:00 2:20 2:40 3:00 3:20 3:40 4:00 4:20

Figure 5

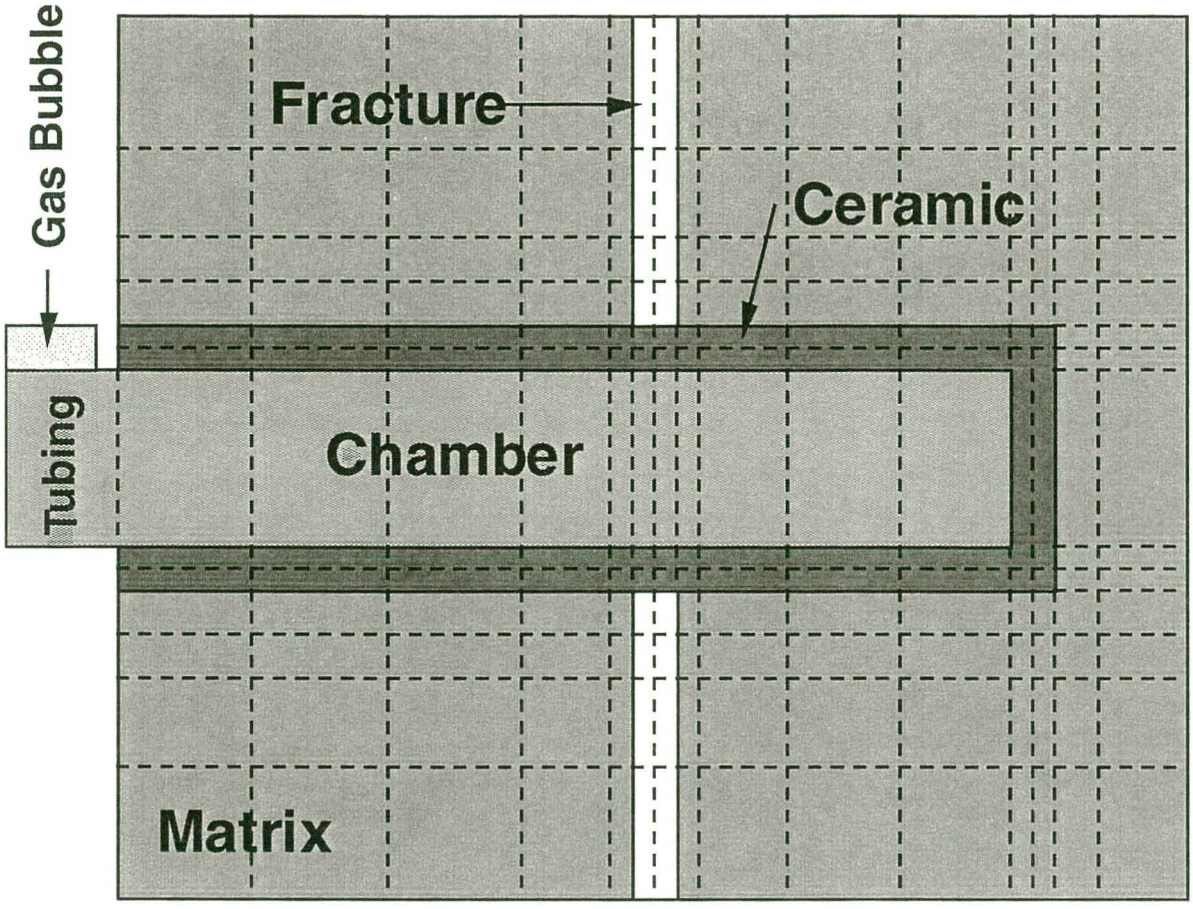

Figure 6.

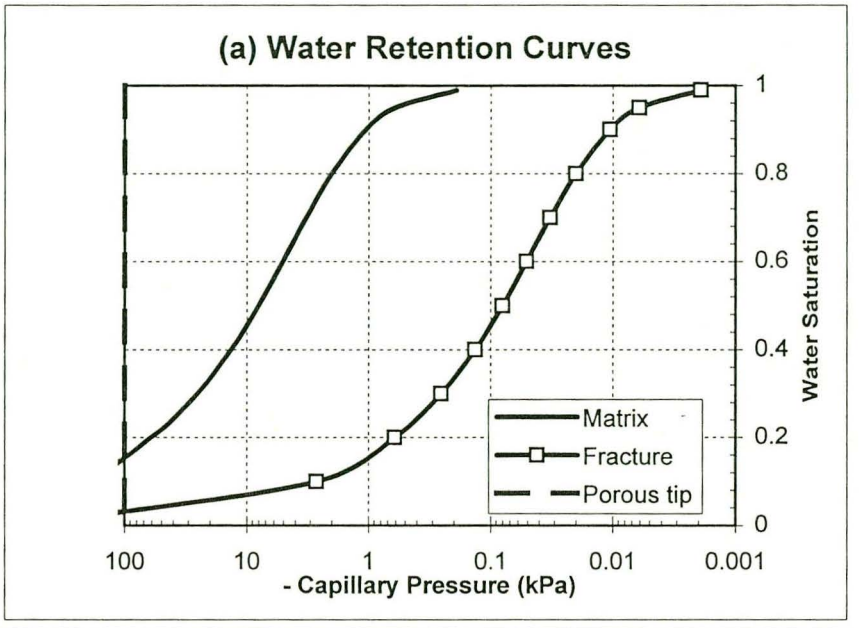
(a) Water Retention Curves
1
0.8
0.6
0.4
0.2
0
Water Saturation
Matrix
Fracture
Porous tip
100
10
1
0.1
0.01
0.001
- Capillary Pressure (kPa)

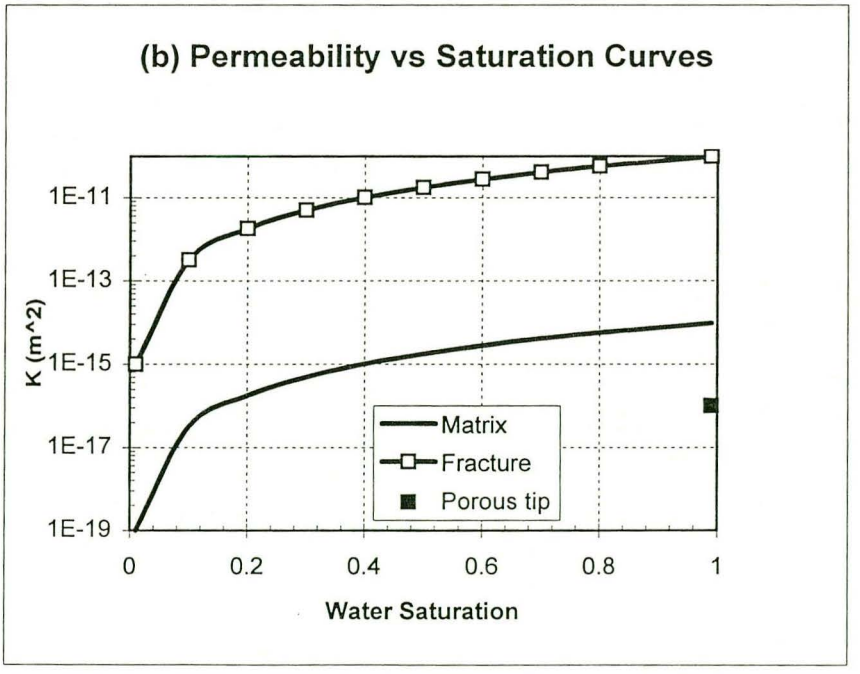
(b) Permeability vs Saturation Curves
1E-11
1E-13
1E-15
1E-17
1E-19
K (m^2)
Matrix
Fracture
Porous tip
0
0.2
0.4
0.6
0.8
1
Water Saturation

Figure 7

(a) Imbibition

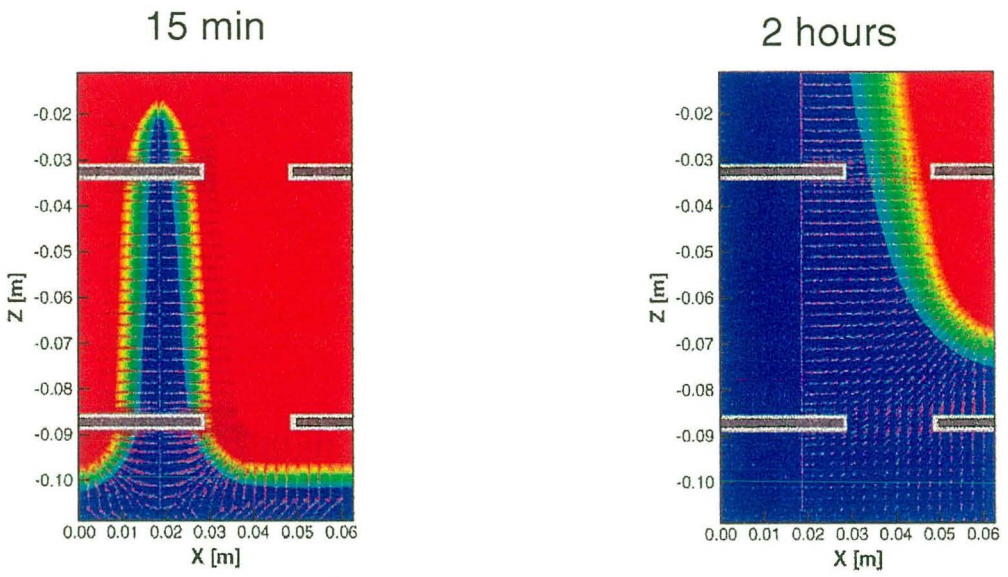

(b) Drainage

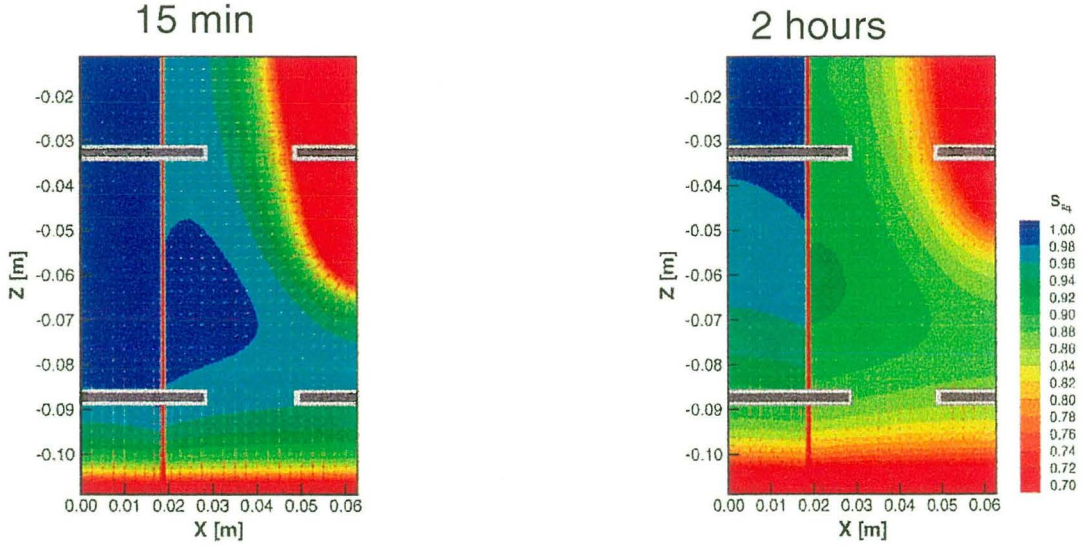

Figure 8

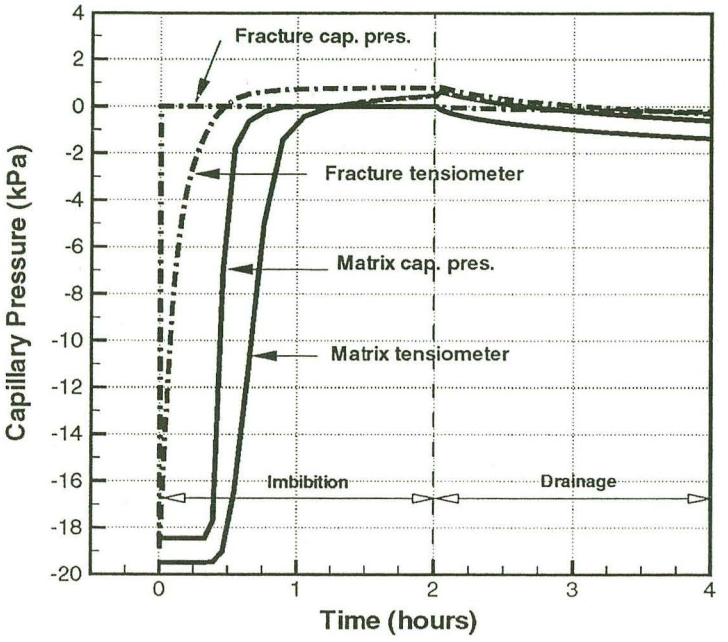
Fracture cap. pres.
Fracture tensiometer
Matrix cap. pres.
Matrix tensiometer
Imbibition
Drainage
Capillary Pressure (kPa)
Time (hours)
4
2
0
-2
-4
-6
-8
-10
-12
-14
-16
-18
-20
0
1
2
3
4

Figure 9

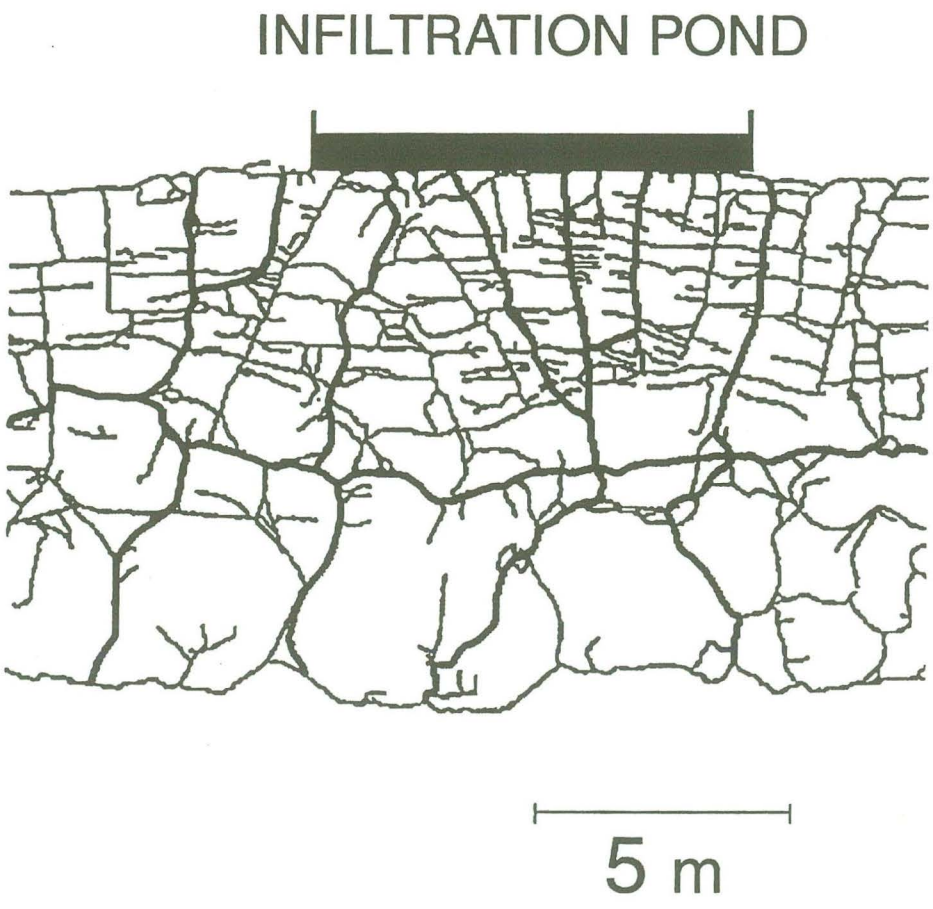

Figure 10

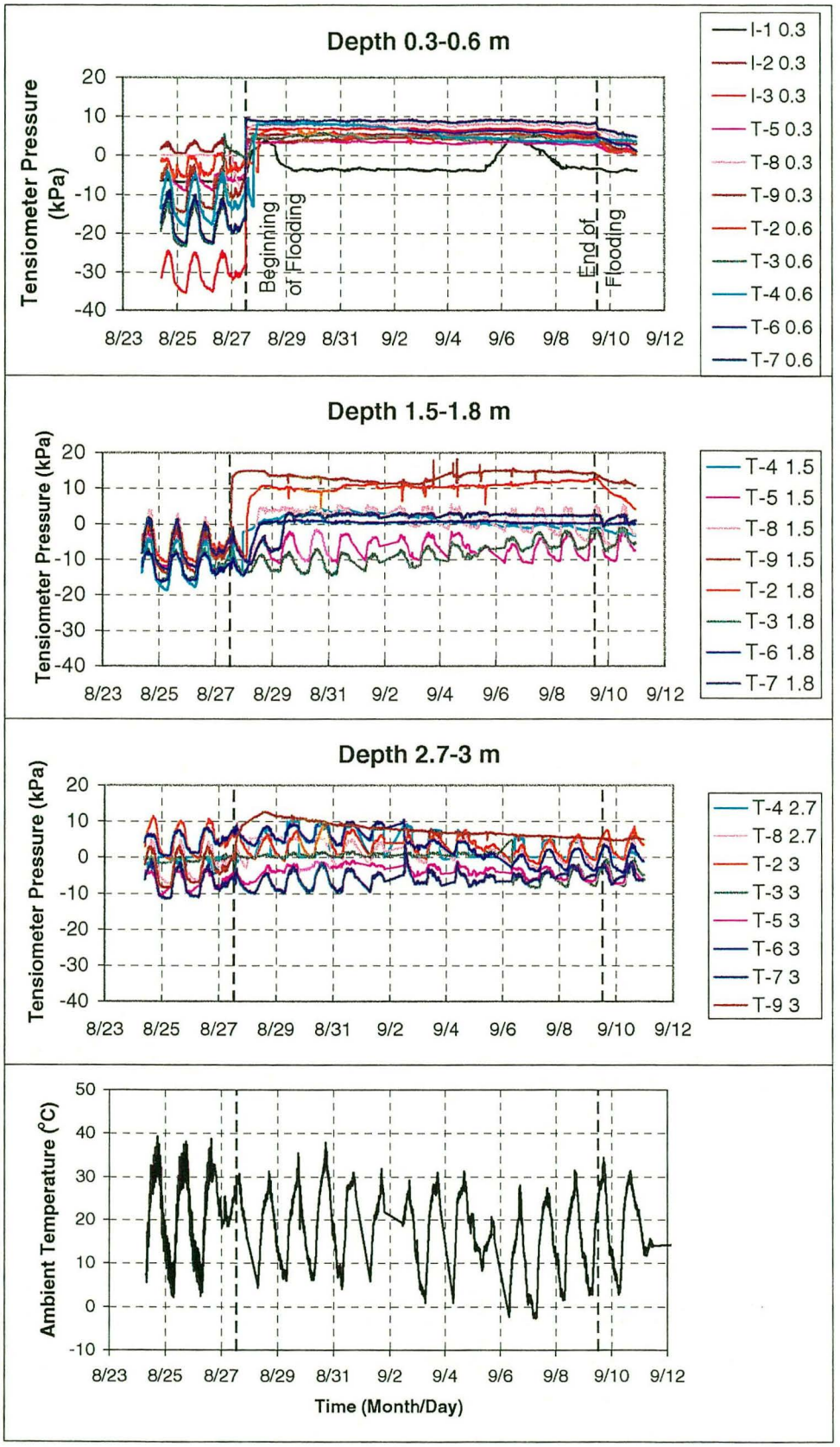
Depth 0.3-0.6 m
Tensiometer Pressure (kPa)
20
10
0
-10
-20
-30
-40
8/23 8/25 8/27 8/29 8/31 9/2 9/4 9/6 9/8 9/10 9/12
Beginning of Flooding
End of Flooding
I-1 0.3
I-2 0.3
I-3 0.3
T-5 0.3
T-8 0.3
T-9 0.3
T-2 0.6
T-3 0.6
T-4 0.6
T-6 0.6
T-7 0.6
Depth 1.5-1.8 m
Tensiometer Pressure (kPa)
T-4 1.5
T-5 1.5
T-8 1.5
T-9 1.5
T-2 1.8
T-3 1.8
T-6 1.8
T-7 1.8
Depth 2.7-3 m
Tensiometer Pressure (kPa)
T-4 2.7
T-8 2.7
T-2 3
T-3 3
T-5 3
T-6 3
T-7 3
T-9 3
Ambient Temperature (°C)
50
40
30
20
10
0
-10
Time (Month/Day)

Figure 11

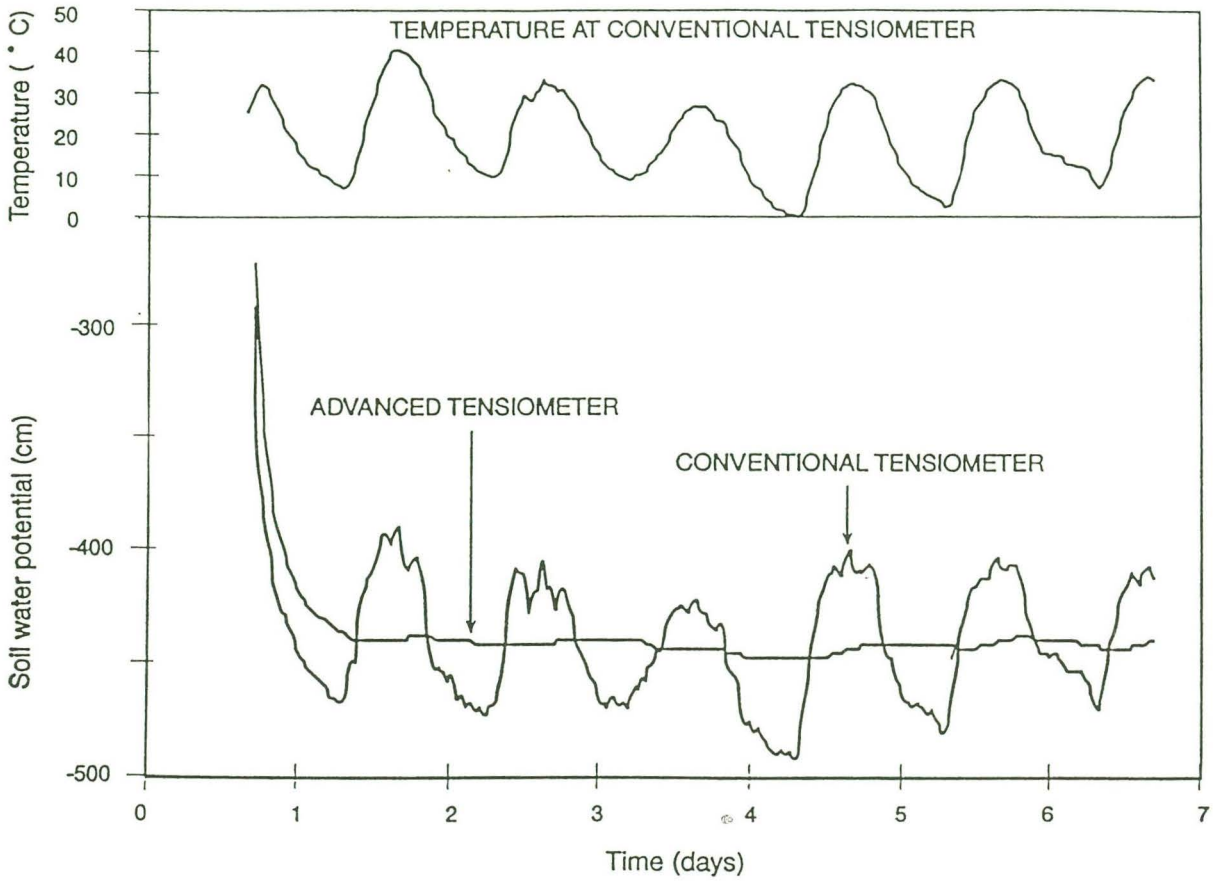
TEMPERATURE AT CONVENTIONAL TENSIOMETER
Temperature (° C)
50
40
30
20
10
0
-300
-400
-500
Soil water potential (cm)
ADVANCED TENSIOMETER
CONVENTIONAL TENSIOMETER
0
1
2
3
4
5
6
7
Time (days)

Figure 12

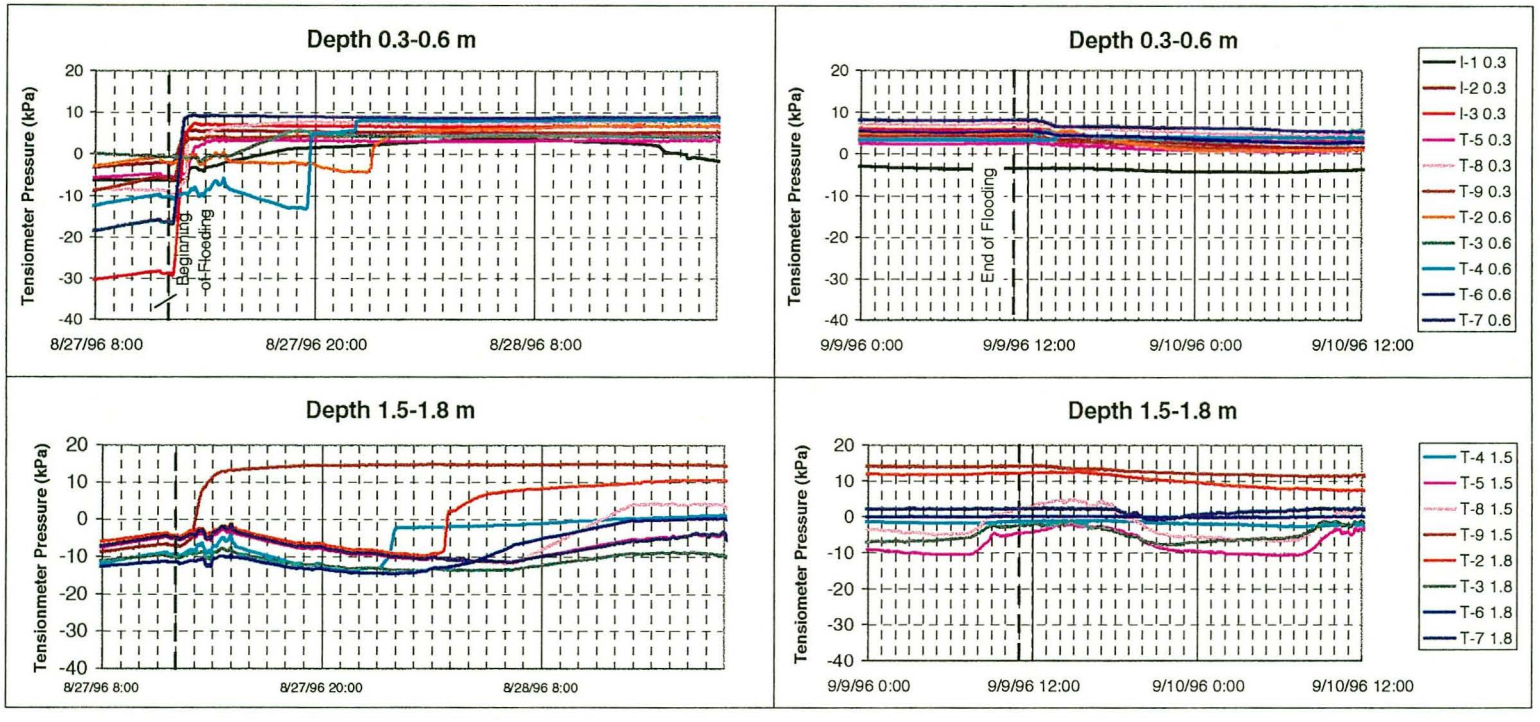
Depth 0.3-0.6 m
Tensiometer Pressure (kPa)
20
10
0
-10
-20
-30
-40
Beginning of Flooding
8/27/96 8:00
8/27/96 20:00
8/28/96 8:00
Depth 0.3-0.6 m
Tensiometer Pressure (kPa)
End of Flooding
9/9/96 0:00
9/9/96 12:00
9/10/96 0:00
9/10/96 12:00
I-1 0.3
I-2 0.3
I-3 0.3
T-5 0.3
T-8 0.3
T-9 0.3
T-2 0.6
T-3 0.6
T-4 0.6
T-6 0.6
T-7 0.6
Depth 1.5-1.8 m
Tensionometer Pressure (kPa)
8/27/96 8:00
8/27/96 20:00
8/28/96 8:00
Depth 1.5-1.8 m
Tensiometer Pressure (kPa)
9/9/96 0:00
9/9/96 12:00
9/10/96 0:00
9/10/96 12:00
T-4 1.5
T-5 1.5
T-8 1.5
T-9 1.5
T-2 1.8
T-3 1.8
T-6 1.8
T-7 1.8

Figure 13

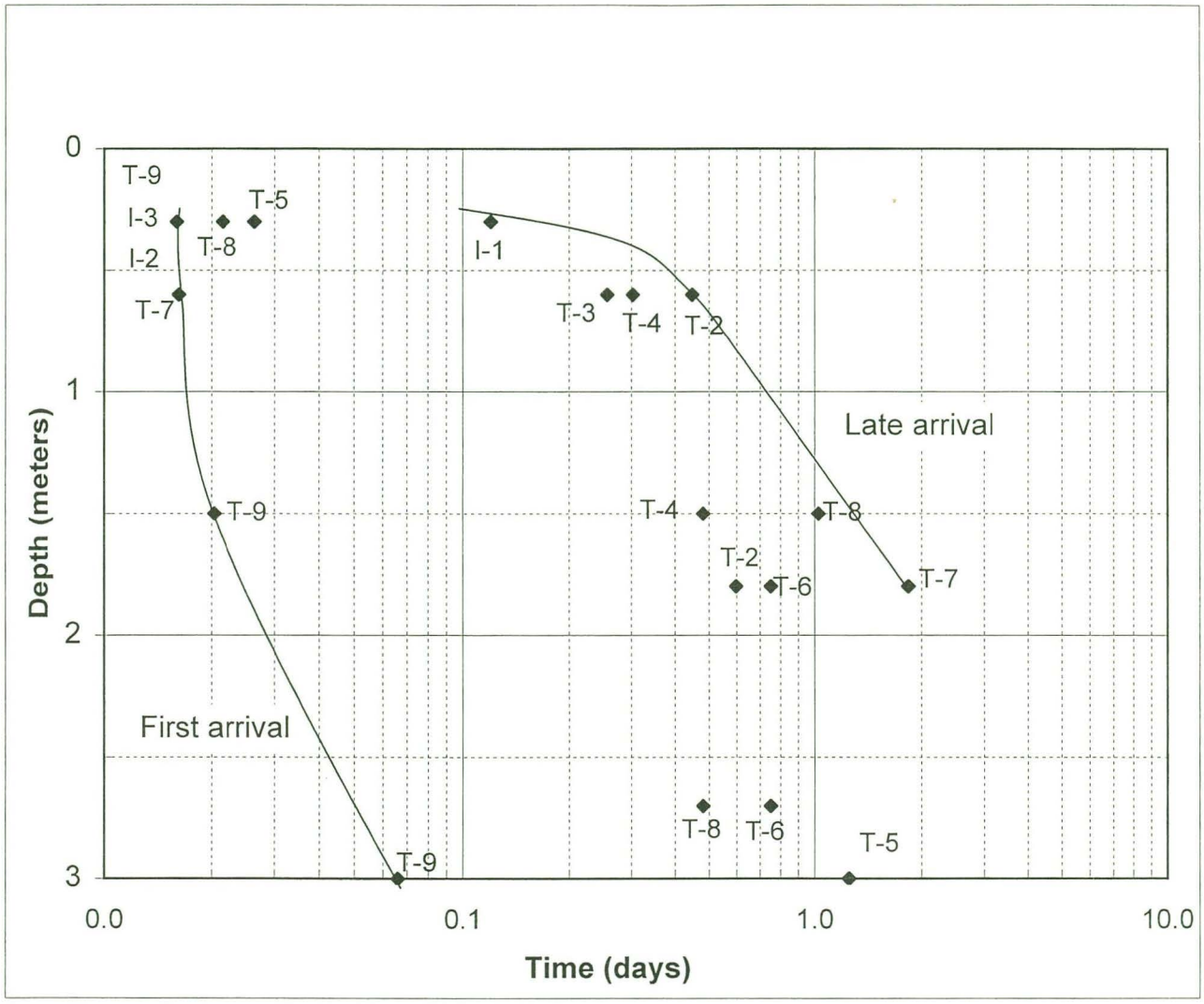
0
1
2
3
Depth (meters)
0.0
0.1
1.0
10.0
Time (days)
T-9
I-3
T-5
T-8
I-2
T-7
I-1
T-3
T-4
T-2
Late arrival
T-9
T-4
T-8
T-2
T-6
T-7
First arrival
T-8
T-6
T-5
T-9

Figure 14

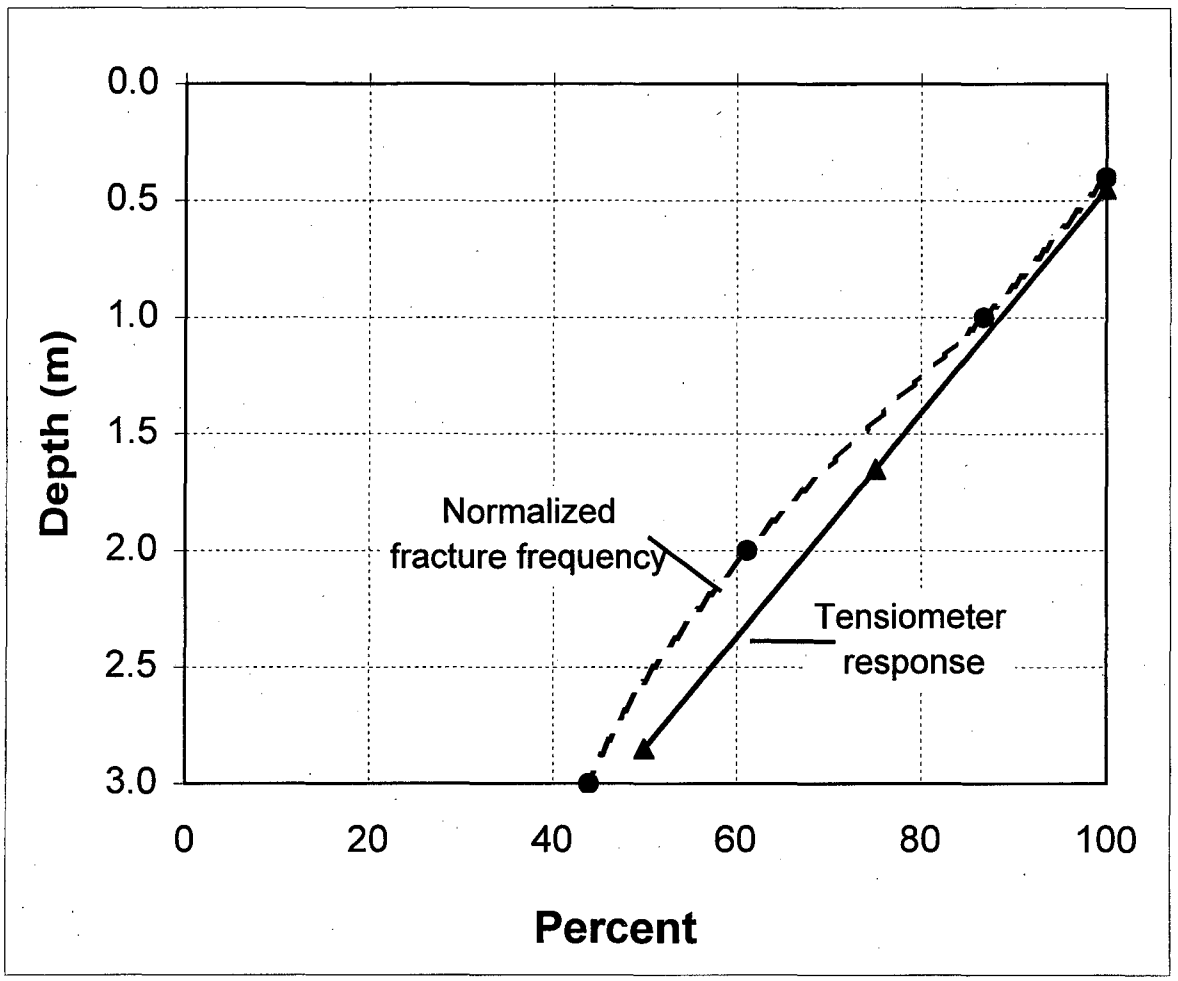
0.0
0.5
1.0
1.5
2.0
2.5
3.0
Depth (m)
Normalized
fracture frequency
Tensiometer
response
0
20
40
60
80
100
Percent

Figure 15

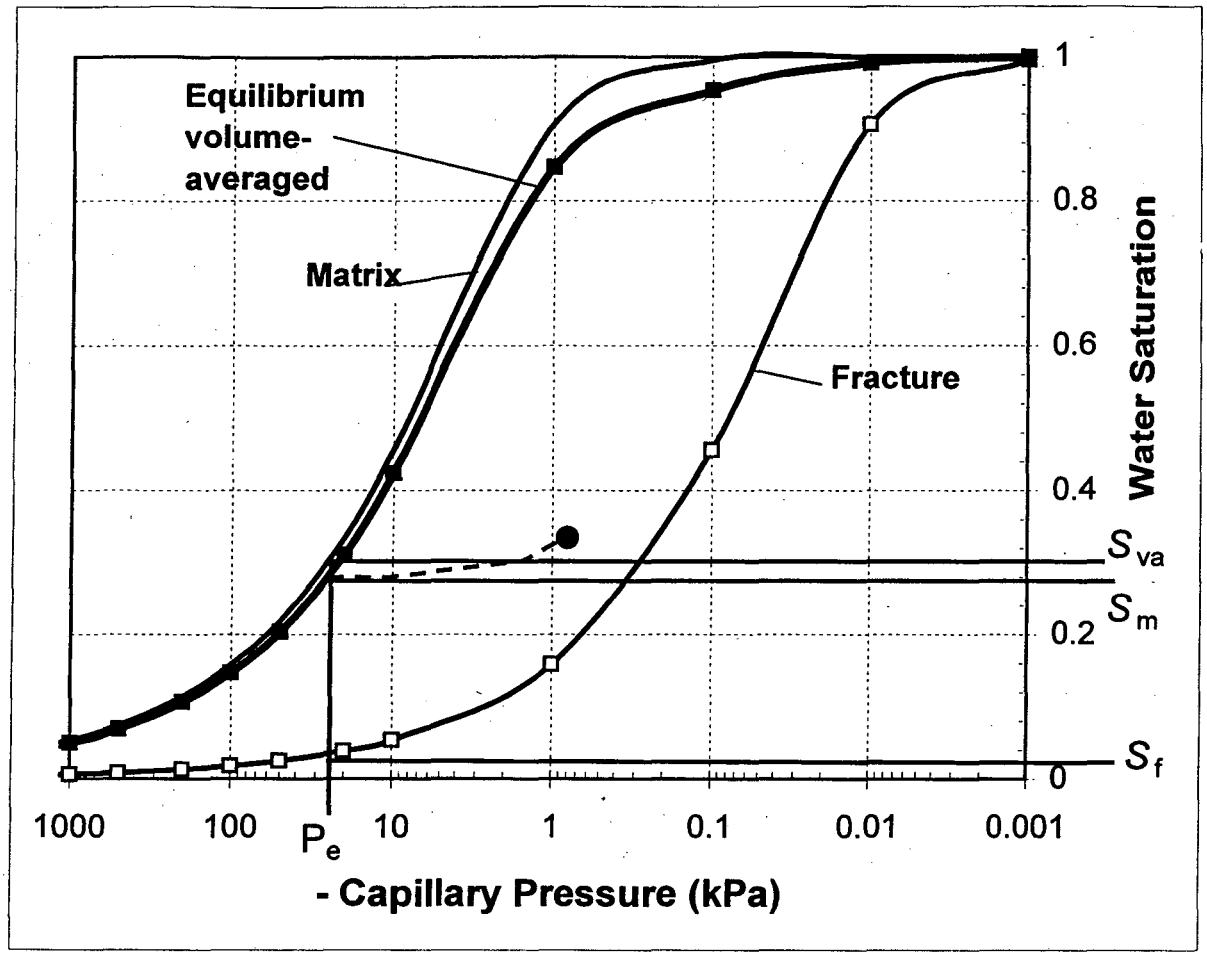
Equilibrium volume-averaged
Matrix
Fracture
1
0.8
0.6
0.4
0.2
0
Water Saturation
S_{va}
S_m
S_f
1000
100
P_e
10
1
0.1
0.01
0.001
- Capillary Pressure (kPa)

Figure 16

ERNEST ORLANDO LAWRENCE BERKELEY NATIONAL LABORATORY
ONE CYCLOTRON ROAD | BERKELEY, CALIFORNIA 94720

Prepared for the U.S. Department of Energy under Contract No. DE-AC03-76SF00098